

Oxide-mediated self-limiting recovery of field effect mobility in plasma-treated MoS₂

Jakub Jadwiszczak,^{1,2,3} Colin O'Callaghan,^{1,2,3} Yangbo Zhou,^{1,2,3,4}

Daniel S. Fox,^{1,2,3} Eamonn Weitz,¹ Darragh Keane,^{2,3,5} Ian O'Reilly,¹

Clive Downing,^{2,3} Aleksey Shmeliov,^{2,3,5} Pierce Maguire,^{1,2,3} John J. Gough,^{1,2} Cormac McGuinness,¹

Mauro S. Ferreira,^{1,2,3} A. Louise Bradley,^{1,2} John J. Boland,^{2,3,5} Valeria Nicolosi,^{2,3,5} and Hongzhou Zhang^{1,2,3,*}

¹*School of Physics, Trinity College Dublin, Dublin 2, Ireland*

²*Centre for Research on Adaptive Nanostructures and Nanodevices (CRANN), Trinity College Dublin, Dublin 2, Ireland*

³*Advanced Materials and BioEngineering Research Centre (AMBER), Trinity College Dublin, Dublin 2, Ireland*

⁴*School of Material Science and Engineering, Nanchang University,
999 Xuefu Road, Nanchang, Jiangxi, China, 330031*

⁵*School of Chemistry, Trinity College Dublin, Dublin 2, Ireland*

Precise tunability of electronic properties of 2D nanomaterials is a key goal of current research in this field of materials science. Chemical modification of layered transition metal dichalcogenides leads to the creation of heterostructures of low-dimensional variants of these materials. In particular, the effect of oxygen-containing plasma treatment on molybdenum disulfide (MoS₂) has long been thought to be detrimental to the electrical performance of the material. Here we show that the mobility and conductivity of MoS₂ can be precisely controlled and improved by systematic exposure to oxygen:argon plasma, and characterise the material utilising advanced spectroscopy and microscopy. Through complementary theoretical modelling which confirms conductivity enhancement, we uncover the role of a two-dimensional phase of molybdenum trioxide (2D-MoO₃) in improving the electronic behaviour of the material. Deduction of the beneficial role of MoO₃ will serve to open the field to new approaches with regard to the tunability of 2D semiconductors by their low-dimensional oxides in nano-modified heterostructures.

THE recent decade has produced intense research into layered two-dimensional nanomaterials, with transition metal dichalcogenides (TMDs) such as MoS₂ being the prime focus in the area of novel nanoelectronics¹⁻⁵. Progress demands that a nanofabrication methodology is developed to control the structure and properties of semiconducting layered crystals so that desired functionalities are obtained for these materials in the future. These may include phase transitions^{6,7} or conductivity modulation for next-generation data storage^{8,9}.

In particular, the interaction of low energy RF-generated plasma ions with MoS₂ has already led to the creation of a multitude of devices, including rectifying diodes, photovoltaics and non-volatile memories¹⁰⁻¹². Plasma power and exposure time have emerged as key variables to delineate between chemical etching and physical sputtering regimes¹³⁻¹⁶. Treatment with oxygen-containing plasma leads to the formation of molybdenum trioxide (MoO₃) centres which have been reported to increase the resistivity of the material and inhibit carrier transport, while retaining relative structural integrity of the now oxide-containing MoS₂ heterostructure^{17,18}. Here we demonstrate the tuning of electrical resistivity of few-layer MoS₂ by treatment with O₂:Ar (1:3) plasma. The field effect mobility, μ_{FE} , of the MoS₂ channel is seen to deteriorate initially but recovers to above-original levels after 6 seconds of exposure to the plasma. The associated electrical conductivity of the devices is noted to increase by an order of magnitude at this stage. Upon further treatment, the conductivity and mobility drop again and no subsequent recovery is seen.

In the limited literature regarding this phenomenon, the reason for the apparent recovery remains under debate¹⁹⁻²¹. In this article, we propose a mechanism of impurity-mediated electrical tuning facilitated by a two-dimensional phase of MoO₃, with advanced spectroscopic and microscopic studies to support electrical characterisation. We infer the presence of this 2D molybdenum trioxide phase, which serves to provide additional charge carriers to the MoS₂ channel at 6 seconds of plasma treatment which increases its conductivity. Complementary mathematical modelling of conductive networks reveals the beneficial effect of the freshly-incorporated oxide in the MoS₂ matrix.

Recent theoretical work has predicted the two-dimensional phase of MoO₃ to be a material with a distinctly high acoustic phonon-limited carrier mobility ($> 3000 \text{ cm}^2 \text{ V}^{-1} \text{ s}^{-1}$)²², while experimental 2D FETs made of sub-stoichiometric exfoliated MoO₃ have reported mobilities far exceeding that of MoS₂ ($> 1100 \text{ cm}^2 \text{ V}^{-1} \text{ s}^{-1}$)^{23,24}. The advantageous effect of the 2D phase of MoO₃ on the electrical properties of MoS₂ may play a key role in the applications of planar heterostructures of layered TMDs in novel electronic devices. Future research into this area must consider the benefits of defect-mediated transport in 2D nanoelectronics.

Recovery of field effect mobility in plasma-treated MoS₂

For the initial plasma exposures, the level of drain-source current for a 4 layer (4L) device varies slightly until 6 seconds, when a significant rise in output current is noted indicating an increase in the conductivity of the

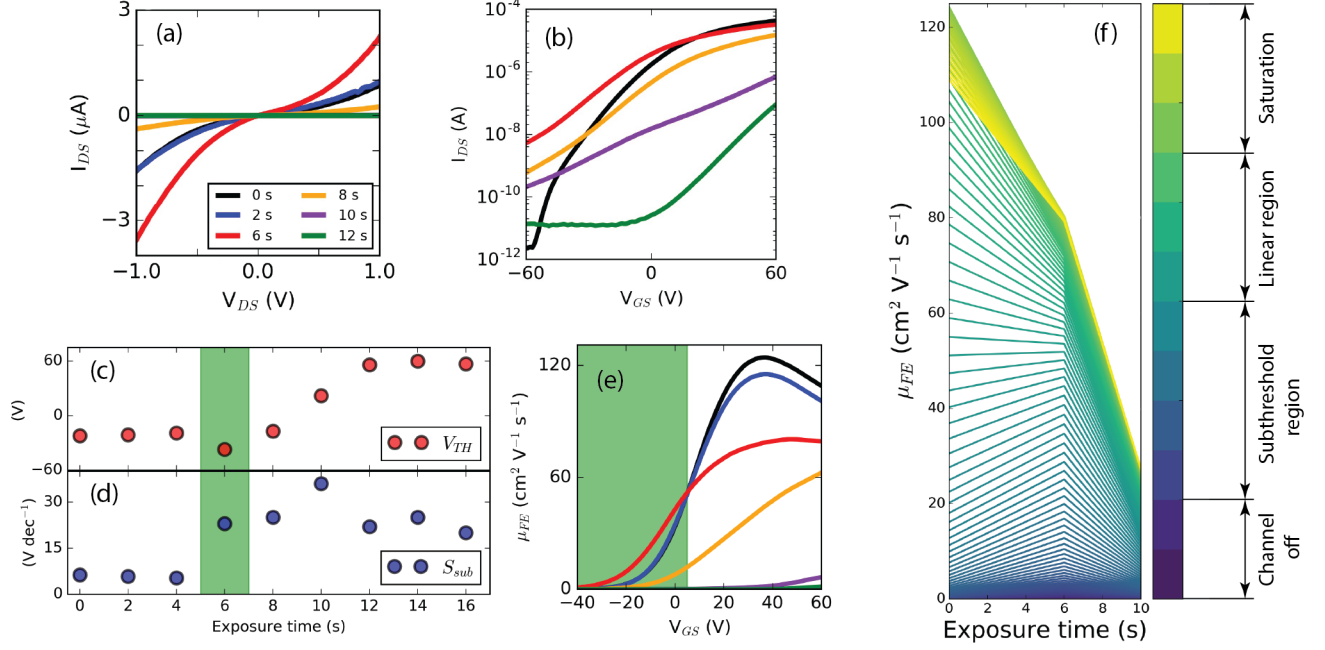


FIG. 1: Note that (a),(b) & (e) share the same color legend. (a) I-V curve evolution over exposure time for a 4L device. All curves are measured at zero gate bias. We note the increased current density observed after 6 seconds (red). (b) Gate sweeps of same device over exposure time. The curves after 6 s, 8 s and 10 s show a largely linear response in the semi-log plot at low gate biases and do not reach threshold over standard sweep range. Subsequent treatment until 12 s drastically shifts V_{TH} to positive gate biases and lowers the current by several orders of magnitude. (c) Threshold voltage for the same device shows a sudden drop at 6 seconds followed by a steady increase to extremely positive gate biases over treatment time. (d) Subthreshold swing variation with exposure time shows a diminished response to the gate field starting at 6 seconds. The area marked in green in (c) & (d) indicates the electrical recovery region. (e) Extraction of field effect mobility for the same 4L device across the whole gate bias range (graph begins from -40 V for clarity). The peak mobility reached in the curves is shown to degrade over time. The green region marks the area of the gate sweep where the 6 s exposure attains highest relative mobility values (red curve). (f) Mobility change over plasma treatment time extracted at gate biases between -60 V and 60 V. The color legend explicitly maps the curves onto different regions of the gate sweep. The increase at 6 seconds is visualised in the form of rising recovery peaks in the body of the plot, which correspond to 6 s mobilities evaluated in the green area marked in (e).

channel (**Fig.1a**). Subsequent exposures cause a continuing drop in current level until the noise floor of the instrument (10^{-11} A) is reached past 12 seconds of plasma treatment. The gate characteristics (**Fig.1b**) of the n-type MoS₂ change significantly after 6 seconds. The level of output current at negative gate values increases by several orders of magnitude at 6 s, implying a drastic shift in the threshold voltage (V_{TH}) to negative gate biases. Correlated with this is the change in the sensitivity of the output current to the applied gate-source bias (V_{GS}), with a much more gradual increase in output current throughout the sweep. **Figures 1c,d** track the evolution of the threshold gate voltage (V_{TH}) and the subthreshold swing (S_{sub}) over plasma exposure time. The threshold voltage is seen to shift from ~ -21 V for the untreated device to ~ -37 V at 6 s of exposure and subsequently to large positive gate biases of ~ 22 V at 10 s and ~ 60 V at > 10 s. The shift towards negative threshold voltages at 6 s implies increased depletion mode functionality for n-type devices, while the upshift

of V_{TH} after further exposure denotes an increase of p-type doping. S_{sub} , in turn, initially shows little change until it increases 5-fold at 6 s and up to 8-fold at 10 s relative to the values before treatment. Upon further exposure, it drops again to ~ 25 V dec^{-1} as V_{TH} is shifted to large positive gate biases. At 6 seconds, all samples show a marked increase in S_{sub} , indicating that they are less sensitive to variations in gate field around the region where the FET conductive channel is formed.

The field effect mobility, μ_{FE} , of the device is plotted as a function of gate bias in **Fig.1e**. The peak value of mobility is seen to drop with exposure time, and the gate bias necessary to reach saturation shifts towards larger V_{GS} . Importantly, for V_{GS} in the region from -60 V to 5 V (highlighted green area in the plot), the mobility at 6 s can now be tuned to much higher values than for the untreated device, with corresponding conductance of the device increasing by over one order of magnitude in this region. Subsequent treatments to 8 s and 10 s decrease μ_{FE} markedly and no recovery is seen beyond this point.

In addition, the change in μ_{FE} over exposure time at each applied gate bias between -60 V and 60 V is charted in **Fig.1f** in 1 V steps. The extracted curves are color-mapped to the palette seen on the right, scaling from extremely low gate biases (-60 V) to extremely high (60 V). Inside the decay envelope of the peak mobility evident from the edge contour of this graph, we observe a series of recovery peaks around the region corresponding to a treatment time of 6 seconds. This recovery is pronounced in the linear regime near V_{TH} , i.e. where μ_{FE} rises above initial values extracted for the untreated device. This corresponds directly to the green region in **Fig.1e** where the red curve (6 s) attains higher values than the other curves, i.e. across $V_{\text{GS}} \in [-60 \text{ V}, 5 \text{ V}]$. The subsequent drop in μ_{FE} and conductance is a direct consequence of material etching and introduction of scattering centres that happens after 10 seconds.

The notable increase in current density seen in **Fig.1a**, the close-to-linear response to the variation in gate bias at 6, 8 and 10 s (red, purple and orange curves in **Fig.1b**), and the increase in S_{sub} all hint at the presence of a highly conductive phase in the material at 6 seconds of exposure, which is responsible for the recovery. In the following sections, we show this phase is a two-dimensional form of MoO_3 produced by a chemical reaction with the plasma.

MoS₂ surface modification by oxygen insertion

We use atomic force microscopy (AFM) to track the thickness variation and surface roughness of the plasma-treated flake. Phase maps of the same region on a 4L flake are shown in **Figs.2a-c**, with notable change in contrast indicating material difference over time. **Fig.2d** charts the change in the edge heights evaluated from line profiles across the edges of 4L and 5L regions (see **Sup-**

plementary Fig. 9). The initial edge height on the 4L portion increases by $\sim 30\%$ from 0 s to 6 s, and on the 5L area by $\sim 10\%$. This is followed by a subsequent drop in height for longer exposure times. The surface roughness (**Fig.2e**) stays constant within instrument precision, and does not vary more than the thickness of one layer of MoS_2 or MoO_3 in the first 8 seconds of exposure.

The peak in edge height at 6 s is a critical point at which the etching mechanism shifts from one largely dominated by chemical oxygen insertion into the lattice, to one where argon-dominated sputtering of material and removal of species from the surface takes over. With increasing dose of the plasma, the integration of oxygen into the mechanically-exfoliated 2H- MoS_2 structure will introduce considerable change; including rearrangement of electronic density and effective lattice deformation which increases the interlayer distance and raises the thickness of the thin $\text{MoS}_{2-x}\text{O}_x$ film^{14,25-28} while forming oxide-containing patches on the surface. These fine oxide patches, spectroscopically determined to exist by Ko et al.²⁹, can be seen in the scanning electron micrograph in **Fig.2g**. The contrast is due to the higher work function of MoO_3 (6.6 eV)³⁰ compared with that of MoS_2 ($\sim 4.04\text{-}4.47$ eV)³¹. The structural modification undergone by the MoS_2 in the plasma chamber can also be linked to the change in its optical contrast over time (see **Supplementary Fig.10**).

In this sputtering-dominated regime, the surface roughness is seen to increase by over 1 nm at 28 seconds of exposure. However, the unchanging surface roughness up until 8 seconds indicates initial direct conversion of MoS_2 into a planar oxide. Most importantly, the edge height trend correlates with the electrical recovery discussed in the previous section, with a peak at 6 seconds.

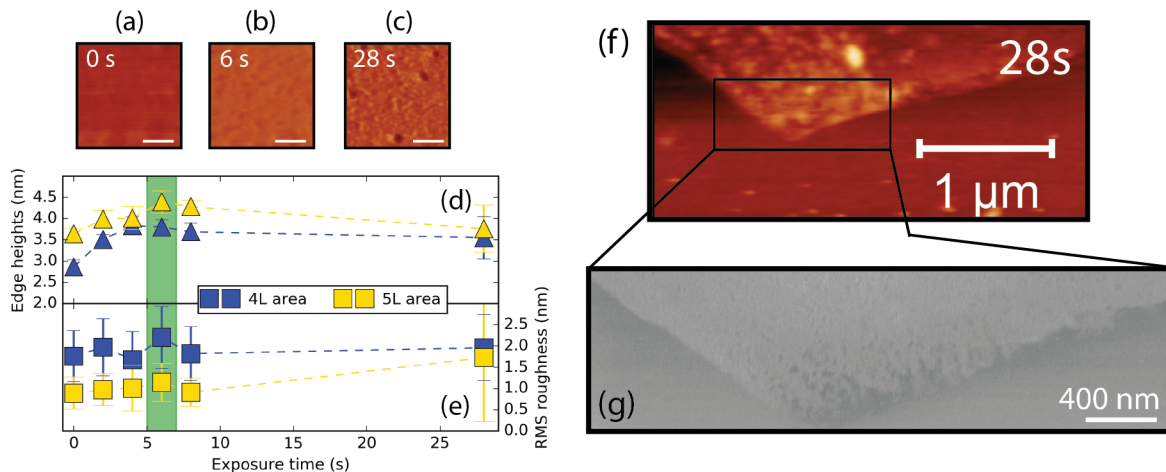


FIG. 2: (a)-(c) Phase maps of the same region of a 4L flake, showing notable corrugation of the surface as oxides are formed over time. Scale bars are all 200 nm. (d) Chart of edge heights extracted along line profiles after each exposure time (see all the raw height maps in Supplementary Fig. 9). The region in green is the edge height peak which correlates with the electrical recovery time at 6 s. (e) RMS surface roughness profiles extracted over time from height maps of the 4L and 5L regions of the flake. (f) AFM map of bottom edge of this flake after 28 s of plasma etching. Visible voids are seen along the bottom of the sample (g) SEM image of the corner of the same flake, exhibiting dark contrast pits on the edge, corresponding to oxidised MoS₂ regions.

Spectroscopic analyses of the surface-bound oxide

We investigate the change to the chemical content of our MoS₂ devices by employing Raman, photoluminescence (PL), energy dispersive X-ray (EDX) and X-ray photoelectron (XPS) spectroscopies. The Raman spectrum (**Fig.3a**) shows notable shifts in the characteristic peaks corresponding to the A₁' mode at ~ 404 cm⁻¹ and the E' mode at ~ 386.0 cm⁻¹ once the sample is exposed to the plasma. Accompanied by a 6-fold decrease in amplitude, the E' peak downshifts to ~ 384 cm⁻¹ while the intensity of the A₁' peak decreases 5-fold and its position upshifts to ~ 410 cm⁻¹, increasing the fitted peak separation from $\Delta\omega = 18$ cm⁻¹ (characteristic for monolayer³²) to $\Delta\omega = 26$ cm⁻¹ (see inset and fits in **Supplementary Fig.12**). The insertion of oxygen into the MoS₂ crystal lattice by the plasma can account for the change in dielectric screening environment and the restoring forces between adjacent MoS₂ molecular layers, thereby affecting the frequencies of both characteristic modes. An increase in $\Delta\omega$ occurs when MoO₃ replaces MoS₂ on the surface of the material^{29,33}. Conversely, the peak separation remains constant or is reduced when no oxides are detected after plasma treatment^{7,28,34}. In addition, the asymmetric peak broadening of both peaks over time

seen in **Fig.3a** has been associated with the presence of additional defect-induced phonons originating from oxide centres in plasma-treated MoS₂²⁹.

The PL intensity is reduced considerably, with a notable shift in peak positions, even just after 2 seconds of plasma exposure (**Fig.3b**). With further exposure, the emission is nearly fully quenched after 8 seconds. The bidirectional shifts of the A peak over time serve to illustrate band structure distortion induced by the plasma treatment. The photoluminescence quenching is due to the defect-induced midgap states that inhibit direct excitonic recombination^{33,35}. The associated quenching rate increases greatly with defect density, inhibiting the radiative recombination completely after 10 seconds of exposure (see **Supplementary Figs.13,14**).

Areal EDX mapping of the MoS₂ flakes (**Fig.3c**) unveils the insertion of oxygen into the MoS₂ structure in a patch-like pattern, as has previously been suggested^{17,36}. We note that plasma exposure time correlates with the gain in the oxygen K_α line relative to the sulfur K_α peak. We plot the relationship of the oxygen and sulfur peak intensities to the plasma exposure time (**Fig.3d**). Oxygen content has increased 3-fold in the first 10 seconds of exposure to the plasma. Importantly, areas high in O signal also show a reduced S signal, suggesting that the oxygen has replaced the sulfur in the MoS₂ lattice through an oxide-forming chemical reaction.

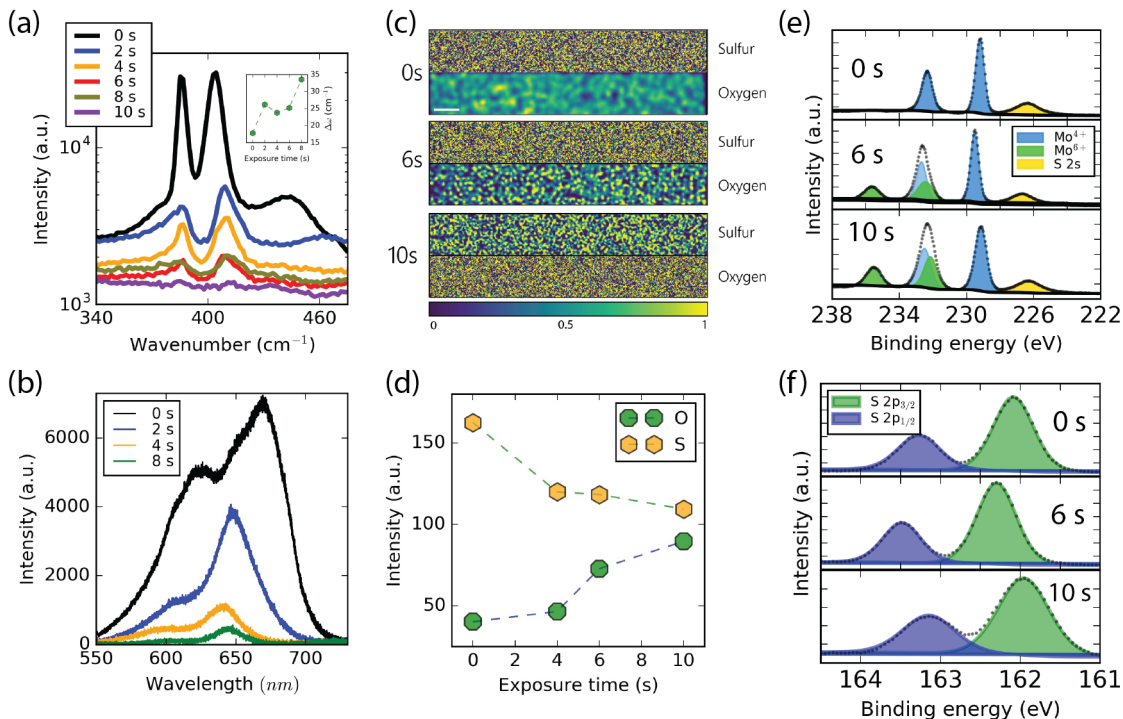


FIG. 3: (a) Raman spectrum of single layer MoS₂ over plasma treatment time shown on semi-log plot. The inset tracks the time evolution of the separation between the E'_1 and A'_1 peaks. (b) PL spectrum of monolayer MoS₂ as it changes over plasma exposure time. (c) Areal EDX mapping of sulfur and oxygen content in the sample at 0, 6 and 10 s of plasma treatment. The colorbar indicates normalised intensity of elemental signal collected at electron beam energy of 5 keV. Scale bar is 200 nm and the same for all maps. (d) Change of EDX intensity from oxygen and sulfur lines over exposure time in the areas shown in (c). (e) XPS spectra of the Mo 3d region showing increased MoO₃ content over time. (f) S 2p region of the XPS spectrum.

Figure 3e shows XPS spectra of the Mo 3d region, indicating the increased presence of oxide species over exposure time. For the pristine sample, the peaks around 229 eV and 232 eV correspond to, respectively, the Mo⁴⁺ 3d_{5/2} and Mo⁴⁺ 3d_{3/2} spin-orbit split components. The 6 s spectrum shows a characteristic Mo⁶⁺ 3d doublet attributed to MoO₃³⁷. After 10 s of exposure, the intensity of the trioxide-associated doublet increases further, with a significant ratio of the surface now containing MoO₃ (estimated at 30-40% from areas of each fitted component). In addition, a thickogram calculation³⁸ reveals that the intensity attenuation of the 10 s spectrum is consistent, within known parameters, with the presence of a bilayer of 2D-MoO₃, i.e. a bulk unit cell of α -MoO₃ on the surface at this exposure time, and 61% of the bilayer of 2D-MoO₃ at 6 s (see details in **Supplementary Section 3**). **Figure 3f** demonstrates the S 2p region. Peak broadening is evident with increased plasma exposure time, indicating a change in chemical order of the surface. Sub-stoichiometric MoS_{2-x} has also been reported to cause the characteristic broadening of the S 2p doublet³⁹, consistent with the picture of sulfur atoms being removed from the surface of the MoS₂ flakes.

Most interestingly, both the Mo 3d and S 2p signals are upshifted after 6 s and downshifted after 10 s. It

is widely accepted that MoO₃ can induce hole doping and concomitant downshifting of the MoS₂ peaks due to Fermi level realignment^{34,36,40,41}. This is in agreement with our transfer curves, with significant threshold voltage shift to positive gate biases at higher plasma exposure times (**Fig.1c**). The upshift at 6 seconds may correlate with the n-type doping observed in the transfer curves in **Fig.1b**.

All the results demonstrate that the plasma-treated MoS₂ undergoes a continuing oxygen insertion and crystal structure distortion. However, plasma-generated MoO₃ is an insulator¹⁷. The electrical recovery at the 6 s mark indicates that an intermediary phase must exist between the pristine MoS₂ semiconductor and the MoO₃-rich insulator. This indicates that the 2D-MoO₃ phase at 6 s is markedly different from its bulk counterpart²².

Nanoscale effects of plasma etching at recovery time

Many etching mechanisms, some contradictory, have been proposed for the surface reaction of oxygen-containing plasma with MoS₂^{7,29,42,43}. To uncover the nature of the elusive two-dimensional oxide phase, we go on to study the effects of the plasma etching on the nanoscale by aberration corrected scanning transmission

electron microscopy (AC-STEM). **Figure 4a** shows a region of a bilayer MoS₂ flake after plasma treatment of 6 seconds. Notable damage occurs to the MoS₂ lattice at this exposure time. Regions of MoS₂ material are completely removed, in nanometre-sized regions. These pits deepen with increasing plasma dose and eventually become perforations. This etching phenomenon is seen to nucleate from individual defective sites, spanning only a few nanometres across. Some of these voids are missing a part of the top molecular layer of MoS₂ after 6 s, leaving behind a bare monolayer region underneath (as confirmed by simulation in **Supplementary Fig 28**).

Large-scale AC-STEM micrographs are presented in **Supplementary Fig.25**. These images were used to obtain statistics on the dimensions of voids formed by the plasma in the MoS₂ at the recovery time. **Figure 4b** demonstrates the distributions of the extracted widths and lengths of imaged voids on the bilayer flake. Yellow (green) histograms show the width (length) distributions. Length is here defined as the largest void dimension, while width is the dimension perpendicular to it. A positive correlation between the lateral dimensions of the etched voids is extracted from data fitting (see

residuals in **Supplementary Fig.29**), showing the close-to-isotropic growth of the voids. The average area of a pore at 6 s is $12.5 \pm 0.1 \text{ nm}^2$. At this time, the relative total percentage area covered by the voids from images sampled in the AC-STEM is $\sim 3.6\%$.

Markedly, the nanoscale EDX and EELS mapping performed with the 60 pm electron beam probe return spectra suggesting very little oxygen presence (see **Supplementary Fig. 33**). It has been demonstrated that oxygen plasma interaction with molybdenum metal leads to the creation of volatile Mo oxides⁴⁴. We find that the plasma-formed oxide phase studied presently is volatile under ultra high vacuum. When the sample is left overnight in the in-situ testing system ($\sim 10^{-9}$ mbar), the n-type depletion mode functionality is reversed by a drastic shift of V_{TH} towards positive gate biases (see **Supplementary Fig. 6**). Similarly, when inserted into the vacuum chamber of the AC-STEM overnight ($\sim 10^{-9}$ mbar), the free-standing flakes lose their weakly-bound surface oxides. The inability to detect oxygen in these atomically-resolved voids leads us to infer that the oxide which was present initially and is responsible for the electrical recovery was sublimated at UHV conditions, leaving behind the underlying MoS₂ structure.

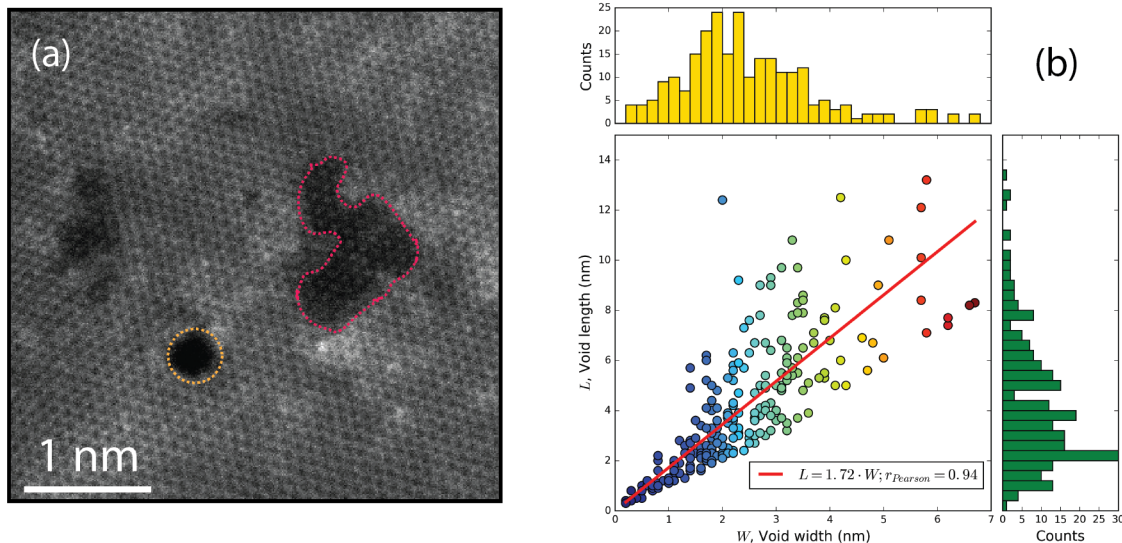


FIG. 4: (a) Typical AC-STEM micrograph showing nanoscale voids forming in bilayer MoS₂ after 6 s of plasma exposure. The region marked in red shows an etched pit with part of the top layer missing. The area marked in orange shows a perforation where no material remains. (b) Scatter plot and histograms visualising the distribution of the lateral dimensions of etched voids on this flake after 6 seconds of plasma exposure. The scatter data are color-mapped from cool to warm with increasing void width.

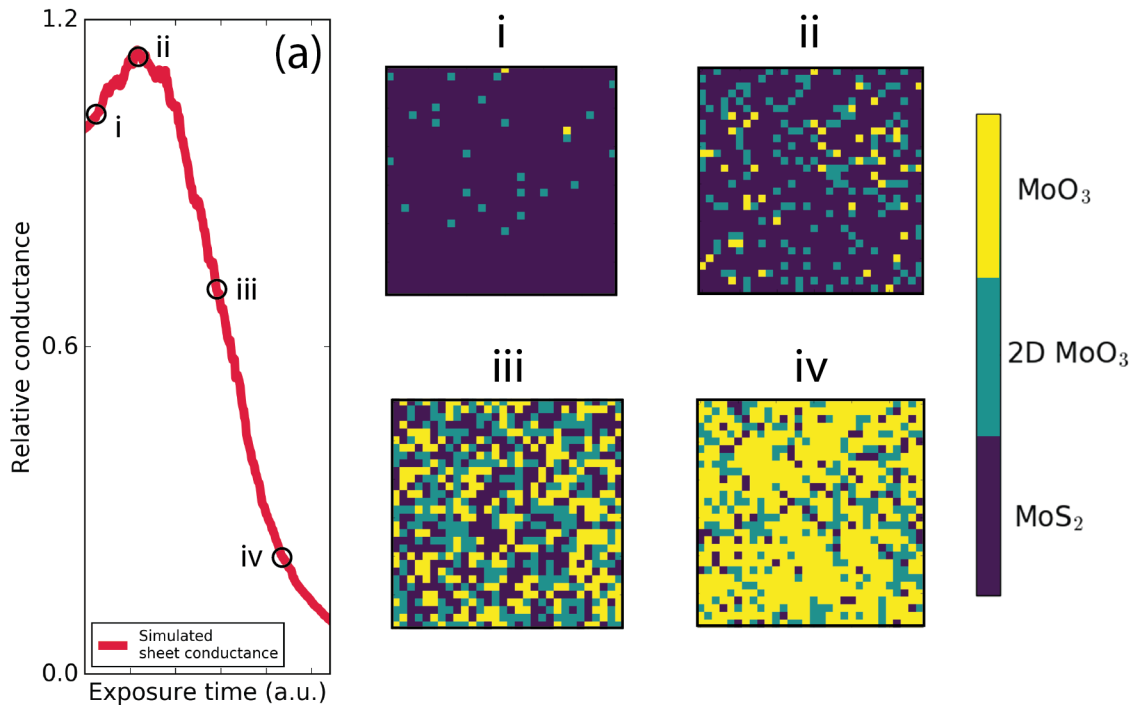


FIG. 5: Simulated sheet conductance of MoS_2 during the progressive conversion from MoS_2 to two-dimensional MoO_3 to MoO_3 . Exposure time, which is in arbitrary units, charts the progress of the plasma-induced chemical oxidation as the simulation is iterated. One site undergoes transformation to the next phase during each iteration. Sites are not destroyed in this simulation, the plasma-etching process finishes when all sites reach the insulating MoO_3 phase. The distribution of phases in the conductive network at four different iteration stages is shown throughout i-iv, where the subsequent phases are color-mapped to the scale shown on the right. The lattice visualised in ii corresponds to the state of the network at the recovery time. The concentration of 2D MoO_3 at that stage is $\sim 15\%$.

Resistive network modelling of conductivity over time

Modelling of classical conductive networks has proven to be an excellent avenue to describe the global conductive properties of nanoscale devices based on local properties of a network^{45–47}. An appropriate conductive network model was thus applied to approximate the effect of plasma-etching on the sheet conductance of MoS_2 . **Figure 5a** shows a plot of the relative conductance of a simulated MoS_2 network, whose nodes undergo conversion to highly conductive 2D- MoO_3 and insulating MoO_3 phases over time (in arbitrary units). The increase in sheet conductance yielded at the start of the simulation qualitatively mirrors the recovery peaks in **Fig. 1f**. This can only be observed if the conductance of the 2D phase is much higher than that of MoS_2 and the relative transition rates between phases follow a relationship such that already defective sites are more likely to convert (see **Methods**). The relative concentration of conductors that exist in each phase is sampled throughout the simulation and visualised through the color-mapped lattices in i-iv. The sheet conductance rises initially as the concentration of 2D- MoO_3 increases. The conductance (and associated field effect mobility) reaches a peak, just as observed in experimental results in **Fig. 1f**, and proceeds to drop off as conductors begin to transition to the insulating MoO_3 .

The differing transition rates affect not only the size of the conductive peak but phase concentrations that it occurs at (see **Supplementary Section 5**). The network map sampled at the conductance peak (ii) shows that the spike in sheet conductance occurs with a relative network coverage of 2D- MoO_3 at approximately 15%. This differs from the experimentally determined areal void coverage of $\sim 4\%$ at 6 s, but remains well under the site percolation threshold for a square lattice⁴⁸. The difference may originate in the underestimation of the area of oxide-born defective sites from AC-STEM images of bilayer flakes. Some voids can become filled with adventitious hydrocarbons over time and/or be obscured by a top molecular layer depending on sample orientation when transferring to TEM grid. This resistive network model demonstrates qualitatively that a highly conductive intermediate oxide phase will serve to facilitate a recovery in the conductance and associated μ_{FE} of a MoS_2 sheet over plasma exposure time.

Outlook and conclusion

We have demonstrated a simple and reliable method to tune the electronic properties of few-layer MoS_2 FETs by using $\text{O}_2:\text{Ar}$ (1:3) plasma. The apparent recovery of electrical conductivity is attributed to the temporary presence of a volatile two-dimensional phase of MoO_3 , whose effect on the performance of the FET is self-limiting as

further exposure results in physical etching and removal of the oxide. We have also inferred the existence of this 2D phase of MoO_3 from evidence collected from advanced spectroscopic and microscopic studies. Additionally, we have demonstrated with a robust simulation that the presence of a conductive phase on the surface of MoS_2 will induce a dose-dependent recovery in the conductance of the material network. Our results are of great importance to groups studying novel 2D TMDs and their low-dimensional oxides for future heterostructure van der Waals devices.

Methods

MoS₂ exfoliation, identification and transfer: MoS₂ flakes were mechanically exfoliated from commercially available bulk molybdenite crystals (SPI Supplies) using the adhesive tape method and deposited on a pre-cleaned Si substrate capped by 285 nm of SiO₂. Samples of up to 10 layers in thickness were identified through optical contrast measurements and Raman spectroscopy. Electron beam lithography was employed to define contacts, followed by deposition of metal film (5 nm Ti/35 nm Au) and lift off in acetone. Suspended MoS₂ samples were prepared utilising the stamp-transfer methodology⁴⁹ to move flakes from substrates onto TEM grids by etching away the SiO₂ surface underneath a polymer-embedded MoS₂ flake.

Plasma treatment: The on-chip MoS₂ FET devices were modified in a Fischione Instruments 1020 plasma cleaner, producing a 13.52 MHz field to ionise a 1:3 mixture of O₂:Ar gas at a constant chamber pressure of ~ 5 mbar. The samples were always exposed to the plasma for 2 seconds at a time, at the same position in the chamber (to within ± 1 mm), to control the accuracy of the experiment. After each exposure, the samples were removed and characterised electrically.

Electrical measurements: The devices were globally back-gated through the highly doped Si substrate and measured in a two-probe configuration at a pressure of 10^{-4} mbar in the vacuum chamber of a scanning electron microscope. The source and drain terminals were provided by tungsten nanomanipulator tips (Imina miBot) connecting the deposited contacts to an Agilent B2912A dual channel sourcemeter.

Microscopy: Transmission electron microscopy was carried out in an FEI Titan 80-300 operated at 300 keV, at a chamber pressure of $4 \cdot 10^{-7}$ mbar. Atomic force microscopy was performed at ambient pressure in an Oxford Asylum system using cantilevers calibrated at 140 kHz. Aberration corrected scanning transmission electron microscopy was carried out in a NION UltraSTEM 200 system operated at 60 keV, at a chamber pressure of $\sim 10^{-9}$ mbar.

Spectroscopy: As sampling efficiency from mechanically exfoliated flakes is extremely low, XPS was performed on larger flakes whose surface (~ 2 mm²)

was plasma-treated in the same way as all FET samples after deposition on Si/SiO₂ substrates. The system utilised a monochromated Al K _{α} X-ray source with an Omicron EA 125 hemispherical analyser set to a pass energy of 19 eV, giving a combined instrumental and source resolution of 0.50 eV. The spectra for these samples were fitted with 2H polytype peaks, as is usual for mechanically exfoliated MoS₂ flakes. PL spectroscopy was performed on substrate-supported flakes using an excitation wavelength of 405 nm. Raman spectroscopy was carried out at atmospheric pressure with a Horiba Jobin-Yvon 488 nm laser equipped with 1200 grooves/mm and a CCD camera. Acquisition time was fixed at 10 acquisitions per second. A 100 \times objective lens was used. The laser spot size was ~ 1 μ m, while the power of the laser was kept below 1 mW. EDX mapping was done on suspended samples using a Bruker Nano XFlash 5030 detector in a Zeiss Supra SEM at 5 keV, with a step size of 0.7nm/px.

Simulation of conductive networks: The computational model begins with a resistive network of identical conductors of magnitude $g_{S_2} = 1$. During each iteration of the simulation, one random conductor transitions from its current phase to the next phase with a certain probability, unless that conductor is already in the final MoO₃ phase. If it does not transition then one of the adjacent sites is chosen and the transition check process is repeated. The probabilities represent the differing transition rates that occur between phases. While the transition rates are experimentally unknown, the assumption is made that they progress such that MoS₂ $\xrightarrow{p_1}$ 2D-MoO₃ $\xrightarrow{p_2}$ MoO₃, where p_1 , p_2 indicate relative conversion probabilities for each process and $p_2 > p_1$. This relationship stems from the fact that the MoS₂ basal plane is chemically unreactive, but any defective nucleation sites will be more likely to facilitate chemical reactions once they are formed⁵⁰. The sheet conductance is then calculated using Kirchhoff's and Ohm's laws (see **Supplementary Section 5**). The iterations are continued until all conductors are in the insulating MoO₃ phase. Iterations in the simulation are a proxy to the plasma-exposure time, with a certain number of phase transitions (or iterations) per unit time.

* hozhang@tcd.ie

¹ B. Radisavljevic, A. Radenovic, J. Brivio, V. Giacometti, and A. Kis, *Nature Nanotechnology* **6**, 147 (2011).

² B. Radisavljevic and A. Kis, *Nature Materials* **12** (2013), 10.1038/NMAT3687.

³ D. Jariwala, V. K. Sangwan, L. J. Lauhon, T. J. Marks, and M. C. Hersam, *ACS Nano* **8**, 1102 (2014).

⁴ D. Lembke, S. Bertolazzi, and A. Kis, *Accounts of Chemical Research* **48**, 100 (2015).

⁵ V. K. Sangwan, D. Jariwala, I. S. Kim, K.-S. Chen, T. J.

Marks, L. J. Lauhon, and M. C. Hersam, *Nature Nanotechnology* **10**, 403 (2015).

⁶ Y.-C. Lin, D. O. Dumcenco, Y.-S. Huang, and K. Suenaga, *Nature Nanotechnology* **9**, 391 (2014).

⁷ J. S. Kim, J. Kim, J. Zhao, S. Kim, J. H. Lee, Y. Jin, H. Choi, B. H. Moon, J. J. Bae, Y. H. Lee, and S. C. Lim, *ACS Nano* **10**, 7500 (2016).

⁸ D. S. Fox, Y. Zhou, P. Maguire, A. O'Neill, C. Ó'Coiléáin, R. Gatensby, A. M. Glushenkov, T. Tao, G. S. Duesberg, I. V. Shvets, M. Abid, M. Abid, H.-C. Wu, Y. Chen, J. N.

- Coleman, J. F. Donegan, and H. Zhang, *Nano Letters* **15**, 5307 (2015).
- ⁹ P. Cheng, K. Sun, and Y. H. Hu, *Nano Letters* **16**, 572 (2016).
- ¹⁰ M. Chen, H. Nam, S. Wi, L. Ji, X. Ren, L. Bian, S. Lu, and X. Liang, *Applied Physics Letters* **103**, 142110 (2013).
- ¹¹ S. Wi, H. Kim, M. Chen, H. Nam, L. J. Guo, E. Meyhofer, and X. Liang, *ACS Nano* **8**, 5270 (2014).
- ¹² M. Chen, H. Nam, S. Wi, G. Priessnitz, I. M. Gunawan, and X. Liang, *ACS Nano* **8**, 4023 (2014).
- ¹³ N.-Y. Cui, N. M. Brown, and A. McKinley, *Applied Surface Science* **151**, 17 (1999).
- ¹⁴ P. D. Fleischauer, *Thin Solid Films* **154**, 309 (1987).
- ¹⁵ J. B. Park, C. B. France, and B. A. Parkinson, *Journal of Vacuum Science & Technology B: Microelectronics and Nanometer Structures* **23**, 1532 (2005).
- ¹⁶ D. Kim, H. Du, T. Kim, S. Shin, S. Kim, M. Song, C. Lee, J. Lee, H. Cheong, D. H. Seo, and S. Seo, *AIP Advances* **6**, 105307 (2016).
- ¹⁷ M. R. Islam, N. Kang, U. Bhanu, H. P. Paudel, M. Erementchouk, L. Tetard, M. N. Leuenberger, and S. I. Khondaker, *Nanoscale* **6**, 10033 (2014).
- ¹⁸ S. I. Khondaker and M. R. Islam, *The Journal of Physical Chemistry C* **120**, 13801 (2016).
- ¹⁹ K.-C. Chen, C.-R. Wu, X.-R. Chang, S.-W. Chang, S.-C. Lee, and S.-Y. Lin, *Japanese Journal of Applied Physics* **55**, 090302 (2016).
- ²⁰ W. Yang, Q.-Q. Sun, Y. Geng, L. Chen, P. Zhou, S.-J. Ding, and D. W. Zhang, *Scientific Reports* **5**, 11921 (2015).
- ²¹ H. Nan, Z. Wu, J. Jiang, A. Zafar, Y. You, and Z. Ni, *Journal of Physics D: Applied Physics* **50**, 154001 (2017).
- ²² W.-B. Zhang, Q. Qu, and K. Lai, *ACS Applied Materials & Interfaces* **9**, 1702 (2017).
- ²³ S. Balendhran, J. Deng, J. Z. Ou, S. Walia, J. Scott, J. Tang, K. L. Wang, M. R. Field, S. Russo, S. Zhuiykov, *et al.*, *Advanced Materials* **25**, 109 (2013).
- ²⁴ M. M. Alsaif, A. F. Chrimes, T. Daeneke, S. Balendhran, D. O. Bellisario, Y. Son, M. R. Field, W. Zhang, H. Nili, E. P. Nguyen, *et al.*, *Advanced Functional Materials* **26**, 91 (2016).
- ²⁵ J. R. Lince, **5**, 218 (1990).
- ²⁶ V. Buck, *Thin Solid Films* **198**, 157 (1991).
- ²⁷ E. Schmidt, F. Weill, G. Meunier, and A. Levasseur, *Thin Solid Films* **245**, 34 (1994).
- ²⁸ R. Dhall, M. R. Neupane, D. Wickramaratne, M. Mecklenburg, Z. Li, C. Moore, R. K. Lake, and S. Cronin, *Advanced Materials* **27**, 1573 (2015).
- ²⁹ T. Y. Ko, A. Jeong, W. Kim, J. Lee, Y. Kim, J. E. Lee, G. H. Ryu, K. Park, D. Kim, Z. Lee, M. H. Lee, C. Lee, and S. Ryu, *2D Materials* **4**, 014003 (2016).
- ³⁰ Y. Guo and J. Robertson, *Applied Physics Letters* **105**, 222110 (2014).
- ³¹ S. Y. Lee, U. J. Kim, J. Chung, H. Nam, H. Y. Jeong, G. H. Han, H. Kim, H. M. Oh, H. Lee, H. Kim, Y.-G. Roh, J. Kim, S. W. Hwang, Y. Park, and Y. H. Lee, *ACS Nano* **10**, 6100 (2016).
- ³² H. Li, Q. Zhang, C. C. R. Yap, B. K. Tay, T. H. T. Edwin, A. Olivier, and D. Baillargeat, *Advanced Functional Materials* **22**, 1385 (2012).
- ³³ N. Choudhary, M. R. Islam, N. Kang, L. Tetard, Y. Jung, and S. I. Khondaker, *Journal of Physics: Condensed Matter* **28**, 364002 (2016).
- ³⁴ H. Zhu, X. Qin, L. Cheng, A. Azcatl, J. Kim, and R. M. Wallace, *ACS Applied Materials & Interfaces* **8**, 19119 (2016).
- ³⁵ N. Kang, H. P. Paudel, M. N. Leuenberger, L. Tetard, and S. I. Khondaker, *The Journal of Physical Chemistry C* **118**, 21258 (2014).
- ³⁶ A. T. Neal, R. Pachter, and S. Mou, *Applied Physics Letters* **110**, 193103 (2017).
- ³⁷ D. O. Scanlon, G. W. Watson, D. Payne, G. Atkinson, R. Egdell, and D. Law, *The Journal of Physical Chemistry C* **114**, 4636 (2010).
- ³⁸ P. J. Cumpson, *Surface and Interface Analysis* **29**, 403 (2000).
- ³⁹ M. Baker, R. Gilmore, C. Lenardi, and W. Gissler, *Applied Surface Science* **150**, 255 (1999).
- ⁴⁰ S. McDonnell, A. Azcatl, R. Addou, C. Gong, C. Battaglia, S. Chuang, K. Cho, A. Javey, and R. M. Wallace, *ACS Nano* **8**, 6265 (2014).
- ⁴¹ S. Chuang, C. Battaglia, A. Azcatl, S. McDonnell, J. S. Kang, X. Yin, M. Tosun, R. Kapadia, H. Fang, R. M. Wallace, and A. Javey, *Nano Letters* **14**, 1337 (2014).
- ⁴² J. Yang, S. Kim, W. Choi, S. H. Park, Y. Jung, M.-H. Cho, and H. Kim, **5**, 4739 (2013).
- ⁴³ L. Tao, X. Duan, C. Wang, X. Duan, and S. Wang, *Chem. Commun.* **51**, 7470 (2015).
- ⁴⁴ T. Saburi, H. Murata, T. Suzuki, Y. Fujii, and K. Kiuchi, *Journal of Plasma and Fusion Research* **78**, 3 (2002).
- ⁴⁵ C. Gomes da Rocha, H. G. Manning, C. O'Callaghan, C. Ritter, A. T. Bellew, J. J. Boland, and M. S. Ferreira, *Nanoscale* **7**, 13011 (2015).
- ⁴⁶ C. O'Callaghan, C. Gomes da Rocha, H. G. Manning, J. J. Boland, and M. S. Ferreira, *Phys. Chem. Chem. Phys.* **18**, 27564 (2016).
- ⁴⁷ J. A. Fairfield, C. G. Rocha, C. O'Callaghan, M. S. Ferreira, and J. J. Boland, *Nanoscale* **8**, 18516 (2016).
- ⁴⁸ T. Gebele, *Journal of Physics A: Mathematical and General* **17**, L51 (1984).
- ⁴⁹ Y.-Q. Bie, Y.-B. Zhou, Z.-M. Liao, K. Yan, S. Liu, Q. Zhao, S. Kumar, H.-C. Wu, G. S. Duesberg, G. L. Cross, *et al.*, *Advanced Materials* **23**, 3938 (2011).
- ⁵⁰ S. KC, R. C. Longo, R. M. Wallace, and K. Cho, *Journal of Applied Physics* **117**, 135301 (2015).

ACKNOWLEDGEMENTS

We are grateful to members of staff at the Advanced Microscopy Laboratory, CRANN, Trinity College Dublin for their continued technical support. We thank C. P. Cullen and S. Callaghan for fruitful discussions regarding XPS. The work at the School of Physics and the Centre for Research on Adaptive Nanostructures and Nanodevices at Trinity College Dublin is supported by Science Foundation Ireland [grant No: 11/PI/1105, 12/TIDA/I2433 07/SK/I1220a and 08/CE/I1432] and the Irish Research Council [grant No: GOIPG/2014/972 and EPSPG/2011/239].

AUTHOR CONTRIBUTIONS

J.J analysed the data, created figures and wrote the manuscript with input from C.O’C and H.Z. I. O’R. discovered the phenomenon. J.J and Y.Z. conducted subsequent plasma exposures and electrical tests. C.O’C. and E.W. carried out the resistor network modelling. Y.Z. performed Raman experiments. P.M. and J.J. carried out SEM imaging and EDX measurements. D.F. and J.J. performed HRTEM and STEM. C.D. acquired AC-STEM images and associated EELS and EDX maps. A.S analysed the AC-STEM results and performed QSTEM simulations. J.J., Y.Z. and J.G. carried out the PL measurements. C. McG. and J.J. performed XPS experiments and analysis. D.K. and J.J. carried out AFM experiments. M.S.F., A.L.B., J.J.B. and V.N. oversaw the experimental work. H.Z. conceived the study and supervised the project. All authors have given approval for the

final version of the manuscript.

ADDITIONAL INFORMATION

Supplementary information containing additional experimental data for each of the sections discussed in this manuscript is available online.

Data availability: Correspondence and requests for materials should be addressed to H.Z. Raw data (code and source data for graphs) generated and/or analysed during the current study are available in the Zenodo repository at: DOI:10.5281/zenodo.809442

COMPETING FINANCIAL INTERESTS

The authors declare no competing financial interests.